Growth and spectroscopic analysis of Yb^{3+}-doped $Y_3Al_5O_{12}$ fiber single crystals

A. Yoshikawa[a)]
Institute of Multidisciplinary Research for Advanced Materials, Tohoku University, 2-1-1 Sendai, 980-8577, Japan

G. Boulon,[b)] L. Laversenne, H. Canibano,[b)] K. Lebbou,[b)] A. Collombet, and Y. Guyot
Physical Chemistry of Luminescent Materials, Claude Bernard/Lyon 1 University, CNRS UMR 5620, Bât. A. Kastler, 10 rue Ampère, 69622 Villeurbanne, France

T. Fukuda
Institute of Multidisciplinary Research for Advanced Materials, Tohoku University, 2-1-1 Sendai, 980-8577, Japan

(Received 31 January 2003; accepted 10 June 2003)

Two major fiber crystal growth methods have been applied for the synthesis and spectroscopic characterizations of Yb^{3+}-doped $Y_3Al_5O_{12}$ (Yb:YAG) to show the feasibility of a flexible single crystal fiber laser. One is the micropulling-down (μ-PD) method and the other is the laser heated pedestal growth (LHPG) method. 500 mm length fiber with no Yb segregation has been grown by the μ-PD method. A detailed analysis of Yb:YAG spectroscopy is made to contribute to the discussion on the determination of energy levels. On the other hand, a combinatorial chemistry approach has been applied on concentration gradient crystal fibers grown by the LHPG method allowing the measurement of the intrinsic radiative lifetime and the analysis of concentration quenching processes of Yb^{3+} ions in YAG. © *2003 American Institute of Physics.*
[DOI: 10.1063/1.1597763]

I. INTRODUCTION

Single crystalline fibers have become the subject of intense study in recent years because of their remarkable characteristics. Specifically, it is motivated by their application to linear and nonlinear optical devices that are not possible in glass fibers. The fiber shape itself is well suited to nonlinear optical interactions, whose efficiencies can be greatly enhanced by the long interaction lengths and tight beam confinement available in guided wave structures. Moreover, the fiber configuration has other advantages. By use as a laser element, it removes heat very efficiently because of the short distance between the pumping region and surrounding temperature.[1] Besides, if we use long interaction length, the concentration of the activator ion can be lower. These factors keep the laser rod at a low temperature, which is preferable for upscaling the output power and it can also minimize the upconversion processes when rare-earth ions are close to each other. As far as using the bulk laser host, it is very difficult to construct a flexible system. For this purpose, the fiber-shaped host material is required (Fig. 1). When we add the fact that it is a single crystal, the properties will shift to a more preferable direction. For example, the thermal conductivity of single crystal is much higher than that of glass. Consequently, a single crystal fiber should be much preferable for high output power applications. Moreover, the laser oscillation efficiency of the single crystal host is also much higher than that of a glass host. At the same time, the small dimensions minimize the occurrence of the defects that are responsible for the low strength of the materials in bulk form.[2]

Taking into account these advantages, we plan to develop a flexible laser system using single crystals fiber. We have choosen yttrium aluminum garnet, $Y_3Al_5O_{12}$ (YAG) as a host material for this fiber laser development project, as it is considered to be the most widely used laser material due to its unusual combination of favorable chemical, optical (isotropic), thermal (high thermal conductivity), and mechanical (robust) properties. Yb^{3+}:YAG has been selected because high average power lasers have gained much attention since the availability of high-power laser diodes. Moreover, a Yb^{3+} activator ion possesses the following advantages from its simple electronic structure:[3–8]

(a) There is no excited state absorption, cross-relaxation process, more up-conversion, or any internal mechanism able to reduce the effective laser cross section.
(b) The intense and broad Yb^{3+} absorption lines are well suited for IR InGaAs diode laser pumping between 900 and 980 nm.
(c) The broad emission band allows the generation of ultra-short pulses.
(d) There is no absorption in the visible range.
(e) A small quantum defect between the absorption and emission wavelengths leads to a low thermal load (11% relative to 30%–40% in Nd^{3+}-doped laser hosts).

[a)]Author to whom correspondence should be addressed; electronic mail: yosikawa@tagen.tohoku.ac.jp
[b)]Also at: Institute of Multidisciplinary Research for Advanced Materials, Tohoku University, 2-1-1 Sendai, 980-8577, Japan.

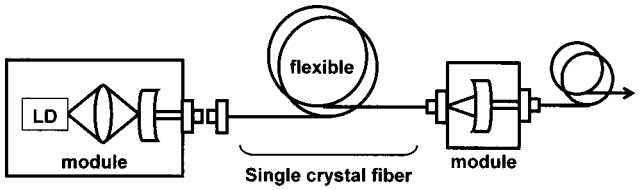

FIG. 1. Schematic of the idea for single crystal fiber laser.

In addition, recently, combinatorial chemistry was adapted to inorganic compounds and was increasingly applied in the study for advanced materials. This systematic, efficient, and fast method was applied to investigate a large field of ternary, quaternary, and high-order solid-state compounds and was tried for superconducting,[9] magnetoresistive,[10] photoluminescent,[11] or catalyst[12] materials. The combination of automated thin-film deposition and physical masking techniques was used for parallel synthesis and has generated a spatially addressable library. As an example, an unusual blue white phosphor (Sr_2CeO_4) with an unexpected structure was discovered from a library of more than 25 000 members.[13] Despite the great number of samples constituting the combinatorial library, this method remains discontinuous. A simultaneous chemical and structural characterization is not associated with the physical property measurement, and the given composition corresponds to the bulk composition without taking into account whether the sample is monophase or not.

A combinatorial approach has been proposed[14] where a rod or a fiber, single crystal or not, with a continuous composition gradient is prepared by using a melting zone technique or a floating zone method. The method is based on the synthesis and investigation of ''concentration gradient fibers or rods'' where composition changes continuously from one end to the other between two well-defined compositions C_A and C_B. If a solid solution exists, a single crystal can be grown with the composition varying continuously between C_A and C_B. The advantage of such samples is that every point of the fiber can be considered as a single crystal where composition and physical properties can be correlated by means of *in situ* measurements. This combinatorial chemistry method has been previously applied to the study of $Yb^{3+}-Er^{3+}$ codoped and Yb^{3+} monodoped sesquioxides.[15–17] We are now dealing with the Yb:YAG system in which we have correlated composition and spectroscopic properties, like Yb^{3+} decay times of the infrared fluorescence, by using concentration gradient monocrystalline fibers.

In this study, the two major fiber crystal growth methods for the single crystal fiber preparation, which we have applied, are described. One is the micropulling-down (μ-PD) method developed at the Tohoku University in Sendai, Japan, and the other is laser heated pedestal growth (LHPG) method which has been developed at the University of Lyonl, France. Structural and spectroscopic characterizations of each kind of samples are analyzed. First, fibers with no Yb^{3+} segregation grown by the μ-PD method will be reported. A detailed analysis of the interpretation of spectroscopic data will be discussed in debate of the accurate position of the Yb^{3+} ion energy levels in the strong vibronic coupling of YAG host. In addition, a combinatorial chemistry approach, which has been applied to concentration gradient crystal fibers grown by the LHPG method, will be reported. The radiative lifetime and the concentration quenching processes depending on the Yb^{3+} concentration will be investigated using the concentration gradient fiber.

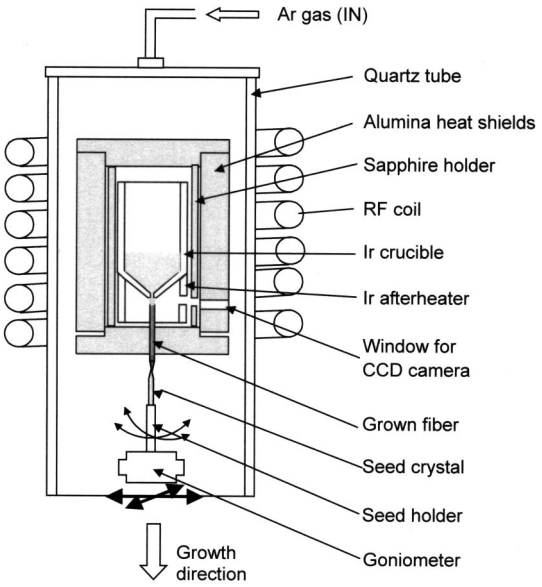

FIG. 2. Schematic of μ-PD furnace around the crucible.

II. EXPERIMENTAL PROCEDURE

A. Fiber single crystal growth procedure

1. μ-PD method

The μ-PD method is one of the fiber crystal growth methods from the melt with the following features:

(1) Starting materials are melted in the crucible; therefore, the homogeneity of the melt is improved by the melt convection. This is the same feature as the Czochralski (CZ) method.
(2) The meniscus is fixed at the edge of the orifice. This makes the crystal growth condition stable. From this point, μ-PD method can be categorized in the edge-defined film-fed growth method. However, if we take the relation between the diameter of capillary channel and diameter of the grown crystal, the situation is different.
(3) The temperature gradient along the growth direction is controllable because of the presence of the after-heater system.
(4) The solute diffusion boundary layer could be as long as desired by adjusting the length of the capillary nozzle, which is free from convection.[18] And the crystal growth velocity could be 10^2-10^3 times higher than that of conventional melt growth method. Both features make $K_{\text{eff}} \sim 1$.
(5) The repeated seeding technique illustrated in Fig. 2 is available to produce few crystals of a similar length without cooling the hot zone to room temperature.

The fiber crystals were grown by the μ-PD method using the setup[19,20] for high melting temperature materials as shown in Fig. 2. Starting materials were prepared by mixing 99.99% pure Al_2O_3, Y_2O_3, and Yb_2O_3 powders produced by High Purity Chemicals Co. at the stoichiometric ratio of $(Y_{0.98}Yb_{0.02})_3Al_5O_{12}$. Mixed powders were cold pressed under the pressure of 3000 kg/cm^2 into disk pellets 15 mm in diameter. The pellets were sintered in a platinum crucible in air for 24 h at 1450 °C. The starting materials were loaded into the crucible. The crucible, about 45 mm in height by 16 mm in diameter, was placed on an alumina pedestal in a vertical quartz tube and was heated using a rf generator.

The crucible temperature was controlled by power of the rf coil. High-density and high-purity (99.7%) alumina ceramic was used to surround the crucible for the thermal insulation. In order to avoid oxidation of the crucible, the crystals were grown in Ar atmosphere (gas flow 1.5–2.0 l/min). The solid–liquid interface was observed using a charge-coupled device camera and monitor. The undoped YAG fibers of about 0.7 mm in diameter produced by the same technique were used as a seed. The crystals were grown at a pulling-down rate of 0.05–10.0 mm/min and were 0.2–1.5 mm in diameter. The best reproducibility of the growth results was found to correspond to a pulling rate of 0.5–1.0 mm/min. The length of the crystals was up to 500 mm which was limited by the length of the pulling system applied.

2. Laser heated pedestal growth method

The LHPG method is one of the most famous fiber crystal growth methods from the melt. It is widely used for fiber crystal growth attempts.[21,22] The LHPG method has the following features:

(1) The starting materials are prepared as a rod shape, and heated by the focused laser. The absence of the crucible makes the material purity high. This is the same feature as the floating zone method.
(2) The meniscus is fixed at the both edges of the seed rod and feed rod; therefore, there are two solid–liquid interfaces.
(3) An extremely high-temperature gradient (in the range of $>10^3$ K cm^{-1}) exists along the growth direction. Therefore, the crystal growth velocity could be 10^2-10^3 times higher than that of conventional melt growth methods, such as the CZ method or Bridgeman method. This feature causes the effective segregation coefficient to tend toward unity.
(4) It is available to apply an electrical field during the crystal growth.
(5) The aforementioned feature allowed the combinatorial approach by using the feed rod with a gradient concentration of the dopant. The dopant composition changes continuously from one end to the other.

When we apply a high growth rate, the composition of the crystallized solid is the same as those of the liquid. A previous study has shown that no segregation appears in the crystallized fiber with a growth rate on the order of 50 mm h^{-1}.[23]

For the preparation of a concentration gradient fiber, the preparation of feed rod is important. As starting powders, Y_2O_3, Al_2O_3, and Yb_2O_3 (99.99% from Rhône Poulenc) were mixed in appropriate quantities. Gradient concentration fibers could be grown from a specially prepared ceramic rod, which already has a varied concentration. The rod is composed of two rods cut along a slant and placed side by side with the dimensions of $1\times1\times30$ mm^3. The rods were cold pressed and sintered at 1300 °C for 12 h.

The pushing rate of the feeding rod was equal to 15–20 mm h^{-1} and the pulling rate of the crystallized rod was at 50–60 mm h^{-1}. All of the crystal growth experiments for concentration gradient fibers were performed in an air atmosphere.

B. Experimental setup for spectroscopic characterization

Absorption spectra were recorded with a spectrophotometer (Cary 2300) equipped with a cryostat allowing measurements between 12 K and room temperature. Excitation of the Yb^{3+} fluorescence was performed with a frequency-doubled Nd:YAG laser (10 ns and 10 Hz) pumping a Quantel three-amplifier-stage dye laser containing a mixture of DCM and LD700 and followed by a hydrogen Raman cell shifter to generate a beam in the 950–980 nm range. The specific infrared fluorescence is selected by using a Jobin Yvon HR250 monochromator fit with a 600 grooves/mm grating blazed at 1 μm and detected by a fast North Coast germanium cell cooled by liquid nitrogen. The signal can be analyzed with the use of a Lecroy 9410 digital oscilloscope coupled to a personal computer.

III. RESULTS AND DISCUSSION

A. Result of fiber single crystal growth

1. Fibers grown by the micropulling down method

Similar to the results of,[24,25] the YAG crystals were slightly faceted with an evident hexagonal cross section that is typical for ⟨111⟩ garnet growth direction. The crystals were transparent and colorless or slightly greenish depending on the Yb^{3+} concentration which cannot be due to either Yb^{3+} or eventual Yb^{2+} ions without any absorption in visible but may be due to traces of other rare-earth impurities, color centers, or oxygen vacancies. The fibers were single phase with a garnet structure. It was confirmed by powder x-ray diffraction analysis. It is pointed out that, in the general case, 100% of the melt was solidified into the fibers. Two fiber crystals, 500 mm in length and 1 mm diameter, were grown from the same melt (nominal composition is $(Y_{0.98}Yb_{0.02})_3Al_5O_{12}$), and were selected for composition and spectroscopic characterization. Grown fiber crystals are shown in Fig. 3.

The composition, as well as the distribution of Yb^{3+} concentration along the growth axis, was measured by electron-probe microanalysis (EPMA) using JEOL (JXA-8621MX). No shifting of the melt composition resulting in second phase formation was observed by EPMA. All of the fibers from the beginning to the end parts of the melt were single garnet phase and no incursion was observed. The re-

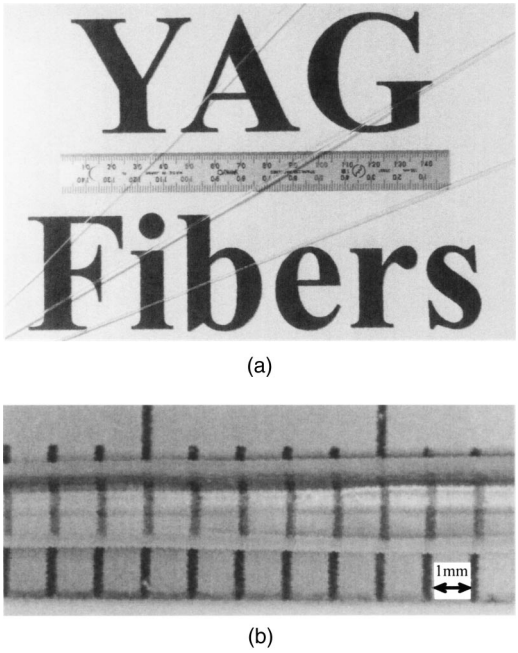

FIG. 3. (a) Photograph of μ-PD grown fibers. (b) Microscopic view of the YAG fiber crystal. Crystal growth rate was 1.0 mm/min.

sults of measurements made along the axial direction are given in Fig. 4. The fiber crystal discussed here was produced at pulling rate of 1.0 mm/min. The distribution of Yb^{3+}-doping cations in the fiber crystals was measured using the electron probe of 10 μm in diameter. The EPMA composition analysis was made with a step of 1.0 mm for the fiber samples as shown in Fig. 4. We could not find any variation of Yb concentration along the growth axis. Taking into consideration the very small amount of Yb in the crystal and corresponding accuracy of the measurements, we can conclude that the axial distribution of the Yb dopant is uniform. Thus, the segregation coefficient of Yb^{3+} in the process described was found to be close to unity: $K_{(Yb^{3+})} \sim 1$.

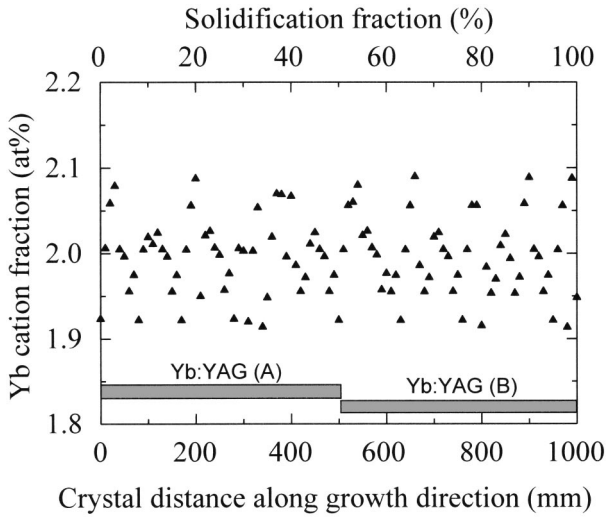

FIG. 4. Distribution of Yb concentration (point data) along growth direction of 2% Yb:YAG fiber crystal. Both Yb:YAG (A) and Yb:YAG (B) were grown from the same melt.

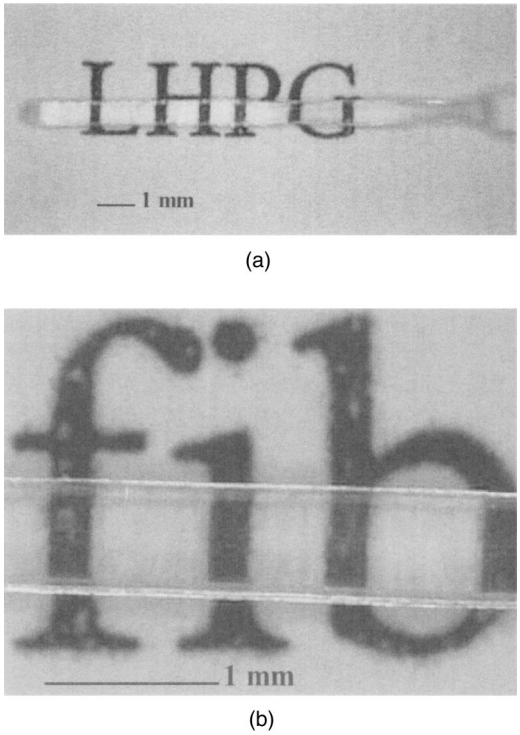

FIG. 5. (a) Photograph of a YAG fiber grown by the LHPG method and (b) microscopic view of the LHPG grown YAG fiber.

2. Fibers grown by the laser heated pedestal growth method

In the melting zone, there is a homogeneous mix of the species in the liquid: The amounts of the solved species vary continuously. When the molten zone moves, the composition gradient is induced in the crystallized rod. By using the gradient concentration ceramic rod, the concentration of the Yb in the melt varies depending on the position of the molten zone.

Concentration gradient fibers with a Yb^{3+} concentration varying up to 10% could be grown. Figures 5(a) and 5(b) show, as an example, photographs of a concentration gradient Yb:YAG fiber. The grown crystal fibers have a typical diameter of about 800 μm and a length of few centimeters. They are crack free, transparent, and free from the visible impurities.

The distribution of cations (Y^{3+}, Yb^{3+}, and Al^{3+}) in the LHPG grown fiber crystals was also measured by EPMA (Fig. 6). We could find the significant variation of Yb^{3+} and Y^{3+} concentration along the growth axis, whereas no variation was found for the Al^{3+}.

B. Spectroscopic characterization

1. Analysis and discussion on the assignment of electronic and vibronic transitions from absorption, emission and Raman spectra

a. Our experimental data. Room-temperature and low-temperature absorption and emission spectra of Yb^{3+}:YAG grown by the μ-PD method are shown in Figs. 7 and 8. Similar results have been obtained with samples grown from the LHPG method. There are clearly many more lines observed than can be accounted for as electronic transitions

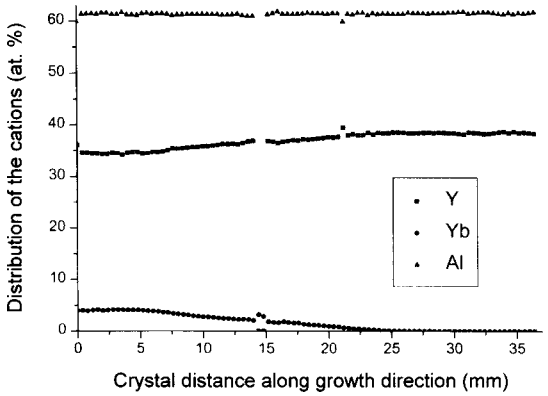

FIG. 6. Distribution of cations along growth direction of concentration gradient (0%–4% Yb) YAG fiber crystal grown by the LHPG method.

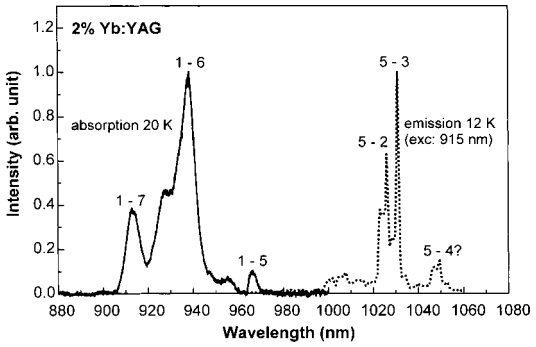

FIG. 8. Absorption spectrum and emission spectrum of 2% Yb^{3+}-doped YAG, grown by the μ-PD method, under 915 nm laser pumping at low temperature.

alone. Although the Yb^{3+} ion has a simple electronic structure with only one excited state ($^2F_{5/2}$) above the ground state ($^2F_{7/2}$), the assignment of pure electronic lines of Yb:YAG, in which Yb^{3+} preponderantly replaces Y^{3+} in *c*-dodecahedral sites of D_2 local symmetry, is a rather difficult task. The degeneracy of the two multiplets is raised and seven Stark electronic levels are expected: Four for the ground and three for the excited state which have been labeled in Fig. 9.

In Fig. 7, the zero-phonon line, which is defined to be the energy separation between the lowest Stark level of each manifold, is easily seen at 968 nm (10 327 cm^{-1}) in coincidence of both absorption and emission spectra. At a low temperature, in Fig. 8, this line is missing due to a strong reabsorption by self-trapping as already observed in Yb^{3+}-doped sesquioxides.[26–28] The absorption cross section is easy to measure from the optical density, thickness, and concentration of the sample whereas the emission cross section can be obtained from the two Fuchtbauer–Ladenburg and reciprocity methods. The reciprocity method, or McCumber method, which has been described in Refs. 3–29 and we have also used in Ref. 8, requires the knowledge of the electronic structure of Yb^{3+} ion and of the absorption spectrum. The emission cross section $\sigma_{(em)}(\nu)$ can be calculated from the absorption cross section $\sigma_{(abs)}(\nu)$ by the following formula:

$$\sigma_{(em)} = \sigma_{(abs)}(\nu) Z_l / Z_u \cdot \exp[E_{(Z_1)} - h\nu/kT].$$

In this equation, $\sigma_{(em)}$ is the emission cross section to be calculated, $\sigma_{(abs)}$ is the absorption cross section, Z_l and Z_u are the lower and upper manifold partition functions, respectively, and $E_{(Z_l)}$ is the zero-phonon line energy. The partition functions Z_l and Z_u have been calculated to be 1.13 and 1.28, respectively, based on the energy level separation values.

The absorption and the emission cross sections of the zero-phonon line have the same value of 0.43×10^{-20} cm^2. The highest values in each spectrum are 0.5×10^{-20} cm^2 in absorption at 943 nm and 2.5×10^{-20} cm^2 in emission at 1030 nm that are within the range reported in literature.[30,31] These two wavelengths correspond at the pumping and the laser wavelengths, respectively, showing the good agreement between results on fibers and those already known on bulky Yb:YAG.

b. Previous assignment. Several reports have been attempted to separate the electronic Stark levels from vibronics but the assignments are still ambiguous.[26–28] The Stark splittings of rare-earth ions are of the order of lattice phonons. If the energy gap between two Stark levels is in near resonance with peaks in the phonon spectrum, the electron–phonon interaction creates modified (nonadiabatic) vibronic states.

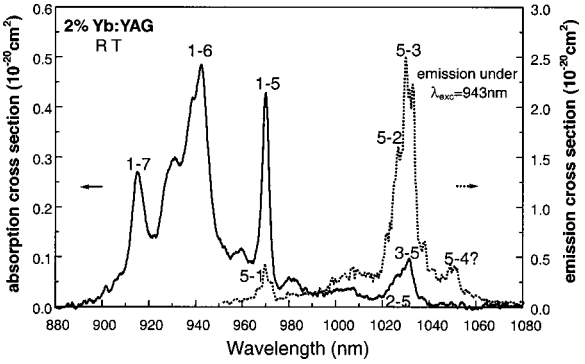

FIG. 7. Absorption spectrum and emission spectrum of 2% Yb^{3+}-doped YAG, grown by the μ-PD method, under 943 nm laser pumping at room temperature. The absorption cross sections (left-hand side, solid line) and emission cross section (right-hand side, dotted line) are given.

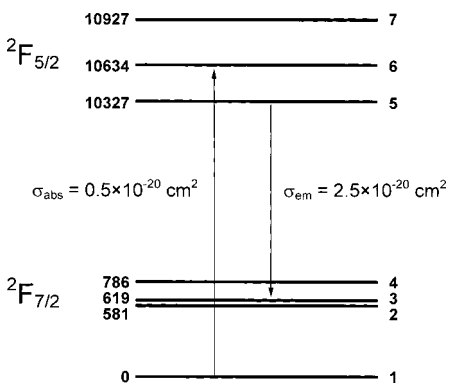

FIG. 9. Attempt of the attribution of the Yb^{3+} energy level scheme in YAG from the spectra of Fig. 8 and the approach of Fig. 10 at low temperature for absorption and emission spectra.

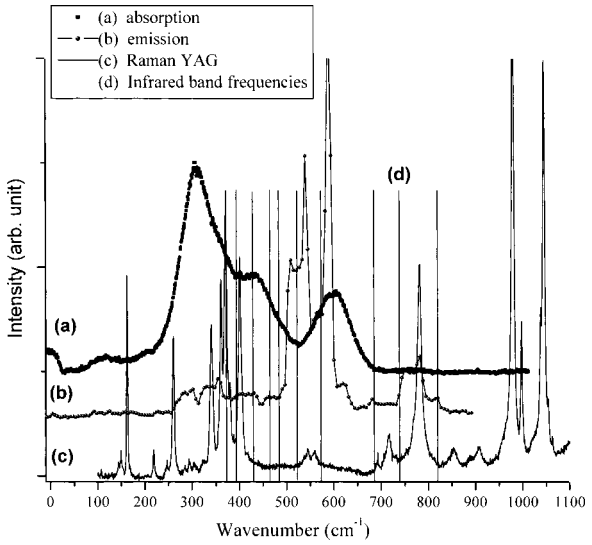

FIG. 10. Comparison of the absorption spectrum, (a), after a rotation of 180°, with the emission spectrum (b) at low temperature (12K), the Raman spectrum (c) and the infrared absorption spectrum represented by vertical lines at room temperature above 370 cm^{-1} and below 820 cm^{-1}. The 1–5 resonant line has been chosen as origin for the absorption and the emission coinciding with the Rayleigh line of the Raman spectrum. The spectral resolution of each used monochromator differs strongly for the four experiments.

This leads to changes in the optical spectral line shapes (broadening, asymmetries, or splitting). Splittings of zero-phonon lines of rare-earth ions could appear if the phonon densities contain sharp peaks and electron–phonon coupling is non-negligible. Such effects have been reported in organic and inorganic compounds, especially for rare-earth ions at the beginning and end of the lanthanide series.[28] Resonant effects could appear for Yb^{3+} in YAG since this ion manifests a strong vibronic coupling and, in YAG, the phonon density presents intense sharp peaks, associated with vibrations of tetrahedral group, as demonstrated by IR, Raman, or vibronic sidebands. By comparing experimental data with theoretical expressions, the positions of the electronic levels and coupling strength have recently been estimated by Lupei *et al.*[26–28] and an electronic energy level diagram for the $^2F_{5/2}$ Yb^{3+} manifold in YAG has been proposed, the positions of the excited Stark levels at 10 327, 10 650, 10 923 cm^{-1}, being shifted from intense absorption lines. The electronic line intensity is shared by divided mixed vibronics created by resonant electron–phonon coupling.

c. Assignment of our spectroscopic data with the help of the Raman spectrum. Since the published data concerning the energy levels of Yb^{3+} in YAG are contradictory, mainly due to a strong vibronic coupling, we have tried to contribute to this debate by again analyzing results in the experimental following approach. We compare absorption, emission, IR absorption, and Raman corrected spectra which have both been drawn in wave number scale, to have at a glance, a quick evaluation of the difference between electronic and vibronic spectroscopic properties. In doing so, we are admitting the hypothesis that Raman and IR absorption spectra should reflect vibronic structure accompanying the main zero-phonon line electronic resonant transition as this is the case with $^2E \rightarrow {}^4A_2$ transition of Cr^{3+}-doped YAG. These spectra were then adjusted in Fig. 10 to the same energy scale, by taking the origin of the absorption and the emission at the zero-phonon line energy, in coincidence with the Rayleigh line of the Ar laser (514.5 nm) used to record the Raman spectrum. In Yb^{3+}-doped oxide crystals, only the lowest level of the $^2F_{5/2}$ excited state is emitting due to fast nonradiative relaxation processes between the three Stark components separated by an energy gap of the same order of magnitude as the phonon energy. Hence, this is the reason why the resonant transition is the best adapted to give a vibronic sideband, on the one hand, in the highest-frequency side (shorter wavelengths) of the absorption spectrum, between 968 nm and 900 nm, and, on the other hand, in the lowest-frequency side (longer wavelengths) of the emission spectrum, between 968 nm and 1100 nm. As such, a symmetric distributions of vibronic lines are expected around a $1 \leftrightarrow 5$ resonant electronic transition. By rotating the absorption spectrum around the origin, we get a direct comparison with the emission, the IR absorption, and the Raman spectra, which are drawn to the lowest-frequency side. Therefore, we should be able to more clearly distinguish electronic and vibronic lines with the advantage to get complementary vibronic spectra from both IR absorption and Raman lines. This is actually our general approach on several Yb^{3+}-doped crystals under analysis in our laboratory applied here especially on Yb^{3+}:YAG for which an analysis has been done in Ref. 32 but by only using expected symmetry of absorption and emission spectra.

In this approach, it can be seen in Fig. 10 that the highest intensity absorption line at 307 cm^{-1} does not overlap either any Raman line or any IR absorption line and can be considered as belonging to an electronic transition. The assignment of this line is probably the $1 \rightarrow 6$ transition. The absorption peak at around 420 cm^{-1} (10 747 cm^{-1}) does not overlap the Raman vibronic spectrum but overlaps with the IR absorption vibronic spectrum and then cannot be asigned to an electronic line but rather to a vibronic line. The difference of the 113 cm^{-1} between the resonant transition 1-6 and the vibronic line is also seen between the resonant transition 1-5 and the nearest line of the absorption spectrum in (a) but is less clear with the other resonant transition 1-7 at 10927 cm^{-1} which is discussed below. This is probably one vibronic frequency belonging to garnet system. By analogy, the peak at around 600 cm^{-1} (10 927 cm^{-1}) overlaps only very weakly with the two Raman lines at around 550 cm^{-1}, and not at all with the IR absorption spectrum. Consequently, it has been associated to the $1 \rightarrow 7$ electronic transition. One can note a strong overlap of the emission spectrum in Fig. 10, with the Raman lines within the range 250–420 cm^{-1} so that this spectral part could be associated with vibronic lines. It seems valuable now to deduce that the level 2 is situated at 581 cm^{-1} (emission line at 1026 nm at room temperature) at a lower energy than the Raman line at 544 cm^{-1}, the Raman line coinciding with an intense emission line, whereas level 3, which is the usual terminal level of the laser transition, could be located very near at 619 cm^{-1} (emission line at 1030 nm at room temperature), in the higher-energy side than the second Raman line near 544 cm^{-1}, in which there is

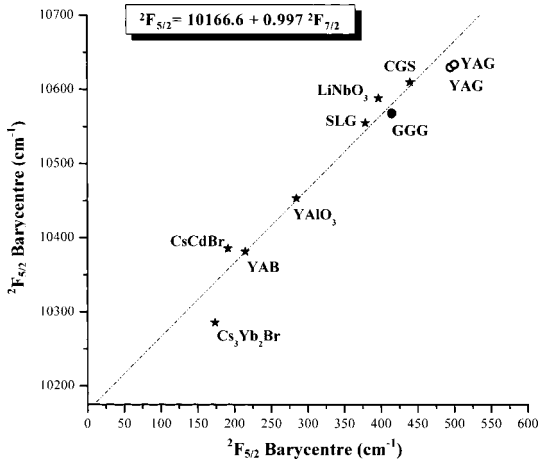

FIG. 11. A plot of the $^2F_{5/2}$ manifold energy barycentre as a function of the $^2F_{7/2}$ manifold energy barycentre for several Yb^{3+}-doped crystals.

no coincidence at all. The proximity of these two levels corresponds to the splitting seen at a low temperature in the highest lines in Fig. 8. Consequently, our interpretation is keeping with the aforementioned remark that the absorption strongest intensity line at 10 628 cm^{-1}, near 940 nm at room temperature, could have a vibronic nature. Moreover, the last line of notable intensity in the emission spectrum at 1044 nm, coincide exactly with an intense Raman line at 781 cm^{-1}. As this emission line is split, our first attempt is to interpret the line of the doublet located at 786 cm^{-1} above the ground state, that is to say at 9542 cm^{-1}, and characterized by the weakest energy located as the $5 \rightarrow 4$ transition. The strong electron–phonon coupling associated with vibrations of tetrahedral group could be responsible for the doublet. As mentioned by Lupei,[28] the near resonance could involve an additional contribution to the linewidth could given by a VanVleck mechanism, that seems important for spin forbidden transitions for ions with small spin–orbit coupling.

d. Use of two independent methods the barycentre plot and the scalar field parameter N_v evaluation. To check the validity and the correctness of our assignment, two methods

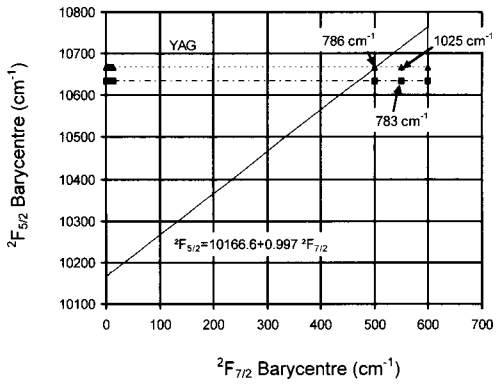

FIG. 12. Positions of the experimental points for the three values [786 cm^{-1} from this work, 1025 cm^{-1} (from Ref. 35) and 783 cm^{-1} (from Refs. 27–29)] of the fourth Stark level energy with respect of the theoretical straight line of the barycentre law. The three values correspond to the energy level values and the arrows indicate the position of the barycentres which do not fit the theoretical straight line for 1025, 786 and 783 cm^{-1} However, the 786 cm^{-1} value is the most valuable one.

can be applied: The barycentre plot[33] and the scalar field parameter N_v evaluation.[34,35]

(i) The "barycentre plot" method, introduced by Antic–Fidancev was applied, based on the fact that the spin–orbit splitting between $^2F_{7/2}$ and $^2F_{5/2}$ is host independent, and equal to the free-ion energy separation. For rare-earth ions, it was shown that the $^{2S+1}L_J$ level barycentre as a function of any other barycentre of an isolated level in the $4f^n$ ground configuration, exhibits a linear dependence within the experimental errors: $^2F_{5/2}=10166.6+0.997\ ^2F_{7/2}$. Especially for Yb^{3+}-doped crystals, when taking the lowest Stark level as the origin of energy and plotting the $^2F_{5/2}$ manifold energy barycentre versus the $^2F_{7/2}$ one (Fig. 11), the representative points generally describe a straight line characterized by a slope of unity. More important is the position of Yb:YAG apparently close to the straight line. However, a zoom around the Yb:YAG point in the straight line shows a slight shift from the theoretical line as can be seen in Fig. 12 either for the position of the fourth Stark component at 783 cm^{-1} or at 1025 cm^{-1}. Even the fourth Stark component at 786 cm^{-1} is slightly outside the theoretical barycentre law quite well. Moreover, we have tried to find other arguments to ascertain such interpretation.

(ii) Using the scalar field parameter N_v, calculated from the respective B_q^k parameters given in literature for 115 different crystals, Auzel has shown that a simple linear relationship between the number of *f* electrons and the crystal field strength can be found. From this result, the maximum splitting of the Yb^{3+} $^2F_{7/2}$ ground state has been derived, assuming a knowledge of the maximum splitting of the Nd^{3+} $^4I_{9/2}$ ground state. Because Nd^{3+} is less prone than Yb^{3+} to mix with vibronics, this approach helps to distinguish the highest Stark level of $^2F_{7/2}$ from vibronics, using the following prediction: The maximum splitting of the $^2F_{7/2}$ Yb^{3+} ground state in a given host site cannot be less than the one of Nd^{3+} $^4I_{9/2}$ in the same crystal host site. For any crystal $\Delta E(7/2) > \Delta E(9/2)$. One prediction is that when the opposite is experimentally found, there is a risk that vibronics have been mistaken for electronic lines. This tool has been used in[35] to predict that the very weak line at 1075 nm, which had been found in Yb:YAG under cathodoluminescence excitation after the multiplication of such signal by 50 in Ref. 32 and attributed to a vibration overtone, might be, in fact, the higher $^2F_{7/2}$ Stark component of Yb:YAG at 1025 cm^{-1} above the ground state, instead of the generally accepted 783 cm^{-1} value (786 cm^{-1} in our work). This assignment has the ability to increase the stark splitting of Yb^{3+} in YAG and so to install the laser crystal among the best ones in the evaluation we have made recently,[6,7] instead to rank it in the lowest compounds of the evaluation. Nevertheless, the fitting of the barycentre plot of the $^2F_{7/2}$ manifold as shown in Fig. 12 is not more accom-

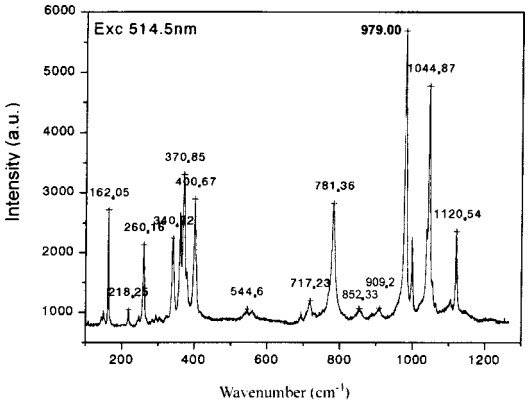

FIG. 13. Raman spectrum of Yb:YAG single crystal fiber at room temperature recorded under Ar laser excitation at 514.5 nm. The main vibronic lines are mentioned.

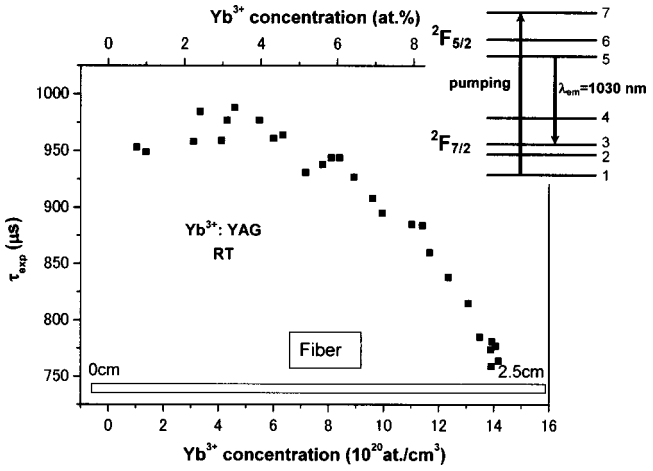

FIG. 14. Room-temperature experimental decay time of the $^2F_{5/2}$ excited state in Yb:YAG concentration gradient fiber, grown by the LHPG method, as a function of the Yb^{3+} concentration.

plished, the experimental point being shifted now to the right energy part corresponding to higher $^2F_{7/2}$ barycentre energy. We can add that in our experiment, this overtone was not detected in the emission spectrum due to a strong noise of the signal within this range. At last, the complete recording of the Raman spectrum, which is reported in Fig. 13, shows strong vibronic lines in YAG at 979, 1000, 1044, and 1120 cm^{-1} respectively, associated also with a smaller intensity peak near 1020 cm^{-1}, which might correspond to the overtone discussed here.

e. Proposition of the Yb^{3+}:YAG energy diagram. Consequently, the applicability of these two methods for Yb^{3+}:YAG cannot give a definitive argument to decide the value of the highest-energy Stark level of the $^2F_{7/2}$ ground state. Without any certain evidence of the real existence of the 1025 cm^{-1} level, we shall continue to adopt the 786 cm^{-1} (783 cm^{-1} in Lupei's interpretation) as the fourth Stark level. Experimental confirmation of the question of the existence of a 1025 cm^{-1} vibration overtone is pending.

Finally, the energy values of the Stark levels of the $^2F_{5/2}$ excited state and the $^2F_{7/2}$ ground state are mentioned as follows in cm^{-1}: $^2F_{5/2}$: 10 327, 10 634, 10 927 (barycentre:10 629) and $^2F_{7/2}$: 0, 581, 619, 786 (barycentre:497). One should be mindful of the energy values in the Lupei's interpretation:[26–28] $^2F_{5/2}$: 10 327, 10 650, 10 923 (barycentre:10 633) and $^2F_{7/2}$: 0, 584, 635, 783 (barycentre:500).

Some differences exist between these values, but the main point is associated with the observation that the highest intensity bands do not correspond systematically to the electronic transitions, Stark levels being shifted from intense absorption lines due to the strong coupling with the host.

2. Radiative lifetime measurement from concentration gradient fiber

The determination of the intrinsic radiative lifetime of Yb^{3+} in crystals requires a lot of precaution. Especially in YAG, measurements of the room-temperature effectively stimulated emission cross section have ranged from 1.6×10^{-20} cm^{-2} to 2.03×10^{-20} cm^2.[36] Depending on the concentration, the self-trapping process is more or less involved. In addition, the high value of the refractive index (1.8), leads to total internal reflection of radiation trapped in the solid for incidence angles greater than 33.7°.[37] The observed measured value of the lifetime is then strongly affected and strongly increased with respect to the intrinsic radiative value.

The measurement of intrinsic lifetimes has received attention for a long time in literature.[38–41] Sumida and Fan[38] measured the lifetime of Yb:YAG for doping levels up to 25 at. %. Their experiment involved using very thin samples of Yb:YAG optically contacted on both sides to larger undoped YAG pieces. The sample was then pumped by a Ti: Al_2O_3 laser tuned to 940 nm with a focused beam spot of 500 μm. Apertures reduced the transverse area seen by the detector, thus minimizing the trapped radiation signal in the plane of the sample. They obtained an intrinsic fluorescence lifetime of 0.951 ± 0.015 ms at room temperature. In Hehlen's experiment,[40] a cubic sample was placed inside a glass sphere filled with index matching oil. This geometry, also suitable for reducing total internal reflection effects, yielded an intrinsic lifetime of Yb:YAG to be 0.9489 ± 0.0006 ms. Recently, powders have been used in a systematic analysis and measurements of materials properties of $(Yb_xY_{1-x})_3Al_5O_{12}$ for nominal x values of 0.05, 0.1, 0.15, 0.18, 0.25, and 0.5, have been reported by Patel *et al.*[37]

Gradient concentration fiber is a unique tool to make the correlation between Yb^{3+} concentration and lifetime measurements which have been measured *in situ* on the same sample in relation to the distance from the top of the crystallized rod. By using a reference made of a homogeneous single crystal fiber of well-defined composition, the two curves were correlated.

The lifetimes have been directly measured on each point of the concentration gradient fiber of 800 μm diameter, with a beam laser of about 500 μm size. Because the volume of materials excited is steady, radiative trapping due to the geometrical effect can be supposed to be characterized by a constant value for each concentration, which should be weak due to the small size of the excited sample. Experimental

lifetime values have been fitted to an unique exponential profile with an excellent agreement. Results are shown in Fig. 14 as a function of the Yb^{3+} concentration. The intrinsic lifetime can be read by follwoing the concentration dependence to the lowest values. The value has been estimated $0.950\ \text{ms} \pm 0.001$, that is to say in the same range as the two others mentioned previously (0.951 and 0.9489 ms, respectively). Better accurate measurements could be possible from the synthesis of a diluted concentration gradient fiber at a lower concentration, let's say, below 3% (4.17×10^{20} atoms/cm^3 Yb^{3+}), and repeating the same approach.

3. Analysis of the concentration quenching process

Identifying the origin of the concentration dependence of the observed experimental lifetime promotes an understanding of excited state dynamics. The curve can be divided into two regimes in Fig. 14:

(i) In the lowest concentration range, up to 3% (4.17×10^{20} atoms/cm^3 Yb^{3+}), the experimental lifetime increases as the dopant concentration increases.

(ii) For the higher concentration range, the measured lifetime decreases when the doping rate increases up to 10% (13.9×10^{20} atoms/cm^3 Yb^{3+}). This concentration range has been taken as an example, but other concentration ranges can be extended up to 100% in the solid solution of the Yb^{3+}-doped YAG garnet.

The two regimes can be assigned in the following way, as was already analyzed in Yb^{3+}-doped sesquioxides:[17]

(i) The first regime is the indication of fluorescence reabsorption, so-called self-trapping process, between 1 and 5 levels, by the $1 \leftrightarrow 5$ resonant transition, giving radiative energy transfer, and then migration of the energy on a long distance increasing the measured lifetime.

(ii) The second regime corresponds to the usual quenching process by energy transfer to defects and other impurities in the host. In the case of Yb^{3+}-doped crystals, because of the presence of only one excited level, we cannot expect the excited state mechanism inside Yb^{3+} ions, which could reach other rare-earth ions by an upconversion process. Only pair emission from two neighbor ions or cooperative emission from aggregates can occur, depending on the shortest distances between Yb^{3+} ions. However, when pair emission is occurring, a very weak signal is detected as observed in Yb: Y_2O_3.[42] The decreased lifetime in the high dopant concentration region can be assigned with a higher probability to an energy transfer through the Yb^{3+} excited ion to impurities. Mainly, two kinds of impurities are observed in YAG: Either rare-earth ions or transition metal ions for which oscillator strengths of the optical transitions in the $3d$ configuration are much higher than those of rare-earth ions in the $4f$ configuration. In our samples, the presence of rare-earth impurities in Y_2O_3 raw material has been observed[42] and the presence of Cr^{3+} ions in Al_2O_3 raw materials has also been detected.[43] All starting materials used in this study have a purity of 99.99%. Because rare-earth elements are chemically related, it is difficult to separate them from each other. On the other hand, Cr^{3+} ions are always detected as impurities in Al_2O_3 raw materials. Thus, impurities are inevitable. Moreover, looking at the Dieke diagram, one can see that many resonant energy transfers are possible between trivalent lanthanide ions. In particular, in the 10 000 cm^{-1} energy range matching with the excited state of Yb^{3+} ions, resonant energy transfer is allowed with the ($^4I_{11/2}$) excited level of Er^{3+} ions. This process is the most known in laser materials and has been recently observed as concentration quenching in sesquioxides[42] and molybdates.[44] As an example, 2% Yb-doped YAG excited under 915 or 943 nm wavelengths, exhibits a green anti-Stokes luminescence visible to the naked eye, with a qualitatively intensity weaker than those of Yb^{3+}-doped Y_2O_3. It was easy to interpret such transitions to Er^{3+} ions and also to see the much weaker signal of Yb^{3+} pair emission by comparing the experimental spectrum with the convoluted one from the IR emission spectrum of Yb^{3+} isolated ions.[42] In YAG, the minimum distance between dopant rare-earth ions substituting Y^{3+} atoms is equal to 3.67 Å, just slightly higher than in Y_2O_3 (C_2 site—C_{3i} site distance = 3.51 Å, and C_2 site—C_2 site distance = 3.53 Å). Consequently, the same type of anti-Stokes emission connected to pairing phenomenon should appear with a lower intensity than in Y_2O_3 due to the higher distances of Yb^{3+} pairs.

Further investigations are needed to elucidate the real role played by both Yb^{3+} pairs and unexpected impurities in concentration quenching mechanisms.

IV. CONCLUSION

Two major single crystal fiber growth methods have been applied on Yb:YAG to show the feasibility of flexible single crystal laser fibers for the development of high average power solid-state lasers under a high-power laser diode. One is the μ-PD method and the other is the LHPG method. Excellent optical quality fiber, 500 mm length, with no Yb^{3+} segregation have been grown by the μ-PD method and then characterized. A deep analysis on the assignment of Yb^{3+} energy levels followed by a detailed discussion have been presented by using an experimental procedure, directly comparing absorption, emission, and Raman spectra in order to distinguish vibronic and electronic transitions. Specifically, we have shown that doubt might subsist on the accurate position of the highest-energy level position of the $^2F_{7/2}$ ground state.

Moreover, a combinatorial chemistry approach has been applied on concentration gradient crystal fibers which are grown by the LHPG method. A concentration gradient method allows the measurement of the Yb^{3+} intrinsic radiative lifetime of 0.950 ± 0.001 ms, in excellent agreement with the already known measurements from more sophisticated techniques. At last, the analysis of concentration

quenching processes of Yb^{3+} ions in YAG have been interpreted as a self-trapping process at a concentration lower than 3% (4.17×10^{20} atoms/cm^3) in competition with both, a nonradiative energy transfer, most probably between Yb^{3+} and unexpected Er^{3+} ions, and a Yb^{3+} ion pairing effect, which has been assigned as responsible for the concentration quenching.

ACKNOWLEDGMENT

The authors wish to acknowledge Y. Murakami of the Laboratory for Developmental Research of Advanced Materials in IMR for the EPMA measurements, as well as the SEM measurement, Professor M. T. Cohen-Adad and Dr. Christelle Goutaudier of the LPCML Laboratory in Villeurbanne and Professor V. Chani of IMR in Sendai for helpful cooperation. This work was partially supported by the Ministry of Education, Science, Sports and Culture, Grant-in-Aid for Scientific Research (B), 12555205, 2000 for one of the authors (A.Y.), and by JSPS-CNRS (France) agreement in Japan. In France, partial support was provided by the ''Groupement de Recherche'' GDR 1148 CNRS LASMAT on Laser Materials and by the ''Relations Internationales'' of CNRS in the framework of JSPS (Japan)-CNRS agreement.

[1] S. Ishibashi, K. Naganuma, and I. Yokohama, J. Cryst. Growth **183**, 614 (1998).
[2] A. P. Levit, *Whisker Technology*, edited by A. P. Levitt (Wiley, New York, 1970), p. 1.
[3] L. DeLoach, S. A. Payne, L. L. Chase, L. K. Smith, W. L. Kway, and W. F. Krupke, IEEE J. Quantum Electron. **29**, 1179 (1993).
[4] L. DeLoach, S. A. Payne, W. L. Kway, J. B. Tassano, S. N. Dixit, and W. F. Krupke, J. Lumin. **62**, 85 (1994).
[5] D. M. Baney, G. Rankin, and K. W. Chang, Appl. Phys. Lett. **69**, 1662 (1996).
[6] A. Brenier and G. Boulon, J. Alloys Compd. **323**, 210 (2001).
[7] A. Brenier and G. Boulon, Europhys. Lett. **55**, 647 (2001).
[8] G. Boulon, A. Collombet, A. Brenier, M.-T. Cohen-Adad, A. Yoshikawa, K. Lebbou, J. H. Lee, and T. Fukuda, Adv. Funct. Mater **11**, 263 (2001).
[9] X.-D. Xiang, X. Sun, G. Briceño, Y. Lou, K.-A. Wang, H. Chang, W. G. Wallace-Freedman, S.-C. Chen, and P. G. Schultz, Science **268**, 1738 (1995).
[10] G. Briceno, H. Chang, X. Sun, P. G. Schultz, and X.-D. Xiang, Science **270**, 273 (1995).
[11] E. Danielson, J. H. Golden, E. W. McFarland, C. M. Reaves, W. H. Weinberg, and X. D. Wu, Nature (London) **389**, 944 (1997).
[12] S. Borman, Chem. Eng. News , 37 (1996).
[13] E. E. Danielson, M. Devenney, D. M. Giaquinta, J. H. Golden, R. C. Haushalter, E. W. McFarland, D. M. Poojary, C. M. Reaves, W. H. Weinberg, and X. D. Wu, Science **279**, 837 (1998).
[14] M. T. Cohen-Adad, L. Laversenne, M. Gharbi, C. Goutaudier, G. Boulon, and R. Cohen-Adad, J. Phase Equilib. **22**, 379 (2001).
[15] L. Laversenne, Y. Guyot, C. Goutaudier, M. T. Cohen Adad, and G. Boulon, Opt. Mater. (Amsterdam, Neth.) **16**, 475 (2001).
[16] L. Laversenne, S. Kairouam, Y. Guyot, C. Goutaudier, G. Boulon, and M. T. Cohen-Adad, Opt. Mater. (Amsterdam, Neth.) **19**, 59 (2002).
[17] L. Laversenne, C. Goutaudier, Y. Guyot, M. T. Cohen-Adad, and G. Boulon, J. Alloys Compd. **341**, 214 (2002).
[18] V. I. Chani, A. Yoshikawa, Y. Kuwano, K. Hasegawa, and T. Fukuda, Extended Abstracts (The 59th Autumn Meeting, The Japan Society of Applied Physics, 15–18 September, 1998, Hiroshima, Japan, 15p-YN.
[19] Y. Kuwano, A. Yoshikawa, V. I. Chani, K. Hasegawa, and T. Fukuda, Proceedings of the 43rd Symposium on Synthetic Crystals, November 12–13 1998, Osaka, Japan, 1A2.
[20] V. I. Chani, A. Yoshikawa, Y. Kuwano, K. Hasegawa, and T. Fukuda, J. Cryst. Growth **204**, 155 (1999).
[21] G. Foulon, A. Brenier, M. Ferriol, M. T. Cohen-Adad, and G. Boulon, Chem. Phys. Lett. **245**, 555 (1995).
[22] K. Lebbou and G. Boulon, *Fiber Crystal Growth from the Melt*, Advances in Materials Research Series, edited by T. Fukuda, P. Rudolph, and S. Uda (Springer, Berlin, 2002).
[23] C. Goutaudier, F. S. Ermeneux, M. T. Cohen-Adad, and R. Moncorge, J. Cryst. Growth **210**, 694 (2000).
[24] S. Uda, J. Kon, K. Shimamura, and T. Fukuda, J. Cryst. Growth **167**, 64 (1996).
[25] A. Yoshikawa, B. M. Epelbaum, T. Fukuda, K. Suzuki, and Y. Waku, Jpn. J. Appl. Phys., Part 2 **38**, L55 (1999).
[26] A. Lupei and V. Lupei, J. Phys.: Condens. Matter **9**, 2807 (1997).
[27] A. Lupei, V. Enaki, V. Lupei, C. Presura, and A. Petraru, J. Alloys Compd. **275**, 196 (1998).
[28] A. Lupei, Opt. Mater. (Amsterdam, Neth.) **16**, 153 (2001).
[29] S. A. Payne, L. L. Chase, L. K. Smith, W. L. Kway, and W. F. Krupke, IEEE J. Quantum Electron. **28**, 2619 (1992).
[30] T. Y. Fan, S. Klunk, and G. Henein, Opt. Lett. **18**, 423 (1993).
[31] P. Lacovara, H. K. Choi, C. A. Wang, R. L. Aggarwal, and T. Y. Fan, Opt. Lett. **16**, 1089 (1991).
[32] R. A. Buchanan, K. A. Wickersheim, J. J. Pearson, and G. F. Herrman, Phys. Rev. **159**, 245 (1967).
[33] E. Antic-Fidancev, J. Alloys Compd. **300**, 2 (2000).
[34] F. Auzel and O. L. Malta, J. Physique **44**, 201 (1983).
[35] F. Auzel, Opt. Mater. (Amsterdam, Neth.) **19**, 89 (2002).
[36] H. W. Bruesselbach, D. S. Sumida, R. A. Reeder, and R. W. Byren, IEEE J. Sel. Top. Quantum Electron. **3**, 105 (1997).
[37] F. D. Patel, E. C. Honea, J. Speth, S. A. Payne, R. Hutcheson, and R. Equall, IEEE J. Quantum Electron. **37**, 135 (2001).
[38] D. S. Sumita and T. Y. Fan, Opt. Lett. **19**, 1343 (1994).
[39] N. Uehara, K. Ueda, and Y. Kubota, Jpn. J. Appl. Phys., Part 2 **35**, L4999 (1996).
[40] M. P. Hehlen, in OSA Proc. Adv. Solid-State Lasers **1**, 530 (1996).
[41] H. P. Christensen, D. R. Gabbe, and H. P. Jenssen, Phys. Rev. B **25**, 1467 (1982).
[42] G. Boulon, L. Laversenne, C. Goutaudier, Y. Guyot, and M. T. Cohen-Adad, J. Lumin. **102-103**, 417 (2003).
[43] Y. Kagamitani, A. Yoshikawa, G. Boulon, and T. Fukuda Abstract Book of the Fourteenth American Conference on Crystal Growth and Epitaxy, Seattle, WA, August (2002), p. 83.
[44] H. Canibano, G. Boulon, L. Palatella, Y. Guyot, A. Brenier, M. Voda, R. Balda, and J. Fernandez, J. Lumin. **102**, 318 (2003).